npj | climate and atmospheric science

Article

Published in partnership with CECCR at King Abdulaziz University

https://doi.org/10.1038/s41612-024-00854-4

Irreversibility of ENSO impacts on the wintertime anomalous Western North Pacific anticyclone to CO_2 forcing

Wen Zhang[1,2], Weichen Tao[1] ✉, Gang Huang[1,2,3] ✉, Kaiming Hu[1,4,5], Xia Qu[1,4], Hainan Gong[4,5], Kai Yang[6] & Ya Wang[5,7]

During the boreal winter, the El Niño-Southern Oscillation (ENSO) influences the East Asia-western North Pacific (WNP) climate by triggering an anomalous WNP anticyclone (WNPAC). Analysis of a suite of coupled model projections under symmetric CO_2 ramp-up (RU) and ramp-down (RD) scenarios, the results reveal that WNPAC strengthens with increasing CO_2 concentrations, peaks early in the CO_2 RD phase, and then gradually weakens without fully returning to its initial state when CO_2 concentrations restore. The irreversible recovery of WNPAC is related to enhanced negative precipitation anomalies in the tropical WNP and positive precipitation anomalies in the equatorial central and eastern Pacific. These changed precipitation anomalies are primarily driven by the climatological equatorial Pacific El Niño-like warming pattern due to various external and internal feedback processes. Our findings indicate that the irreversible change of WNPAC to CO_2 forcing may hinder the winter monsoon and exacerbate climate risks in the East Asia-WNP region.

The El Niño-Southern Oscillation (ENSO) is the dominant mode of interannual climate variability, significantly influencing global climate by altering atmospheric circulations and establishing teleconnection patterns[1–7]. During the El Niño developing fall, an anomalous lower-tropospheric anticyclone emerges over the western North Pacific (WNP) and can persists into the subsequent summer, known as the western North Pacific anomalous anticyclone (WNPAC)[8–13]. The WNPAC plays a pivotal role in mediating ENSO's climatic impact on the East Asia and WNP by modulating monsoon, leading to notable anomalies in temperature and precipitation[14–19].

The maintenance mechanisms of the WNPAC during El Niño mature winter are primarily governed by convective activity anomalies in both the equatorial central and eastern Pacific (CEP) and the tropical WNP. According to the Gill model[20], ENSO-related positive precipitation anomalies in the equatorial CEP can induce cyclonic circulation anomalies as a Rossby wave response to the northwest. Anomalous northeastern winds on the western flank of the cyclonic circulation anomalies transport dry air into the tropical WNP, suppressing local convection[21], and then the anomalous WNPAC is triggered as a Rossby wave response to these negative precipitation anomalies[8,14]. Simultaneously, the northeasterly wind anomalies enhance the northeasterly trade winds, reinforcing local cold sea surface temperature (SST) anomalies through increased evaporation[8]. These cold SST anomalies further suppress local convection and strengthen the WNPAC to form positive thermodynamical feedback. The combined effects of remote forcing from the equatorial CEP and local air-sea interaction in the tropical WNP are supported by numerical experiments[22–24]. Besides, from the perspective of large-scale zonal circulation adjustment, enhanced convection in the equatorial CEP shift the Walker circulation eastward, resulting in reduced precipitation anomalies over the tropical WNP[22,25–31], and thereby influencing the WNPAC. Even under global warming scenario, the precipitation anomalies in the equatorial CEP and the tropical WNP still dominate the variations of the WNPAC during El Niño mature winter[32].

Since the Industrial Revolution, the rise in anthropogenic Carbon Dioxide (CO_2) concentrations has driven long-term global warming, leading to various climate impacts and an increase in the frequency and severity of extreme weather events[33–41]. To address these potential threats, the Paris Agreement aims to limit global temperature increases to below 2 °C relative to pre-industrial levels, with efforts to further constrain the rise

[1]State Key Laboratory of Numerical Modeling for Atmospheric Sciences and Geophysical Fluid Dynamics, Institute of Atmospheric Physics, Chinese Academy of Sciences, Beijing, China. [2]University of Chinese Academy of Sciences, Beijing, China. [3]Laboratory for Regional Oceanography and Numerical Modeling, Qingdao National Laboratory for Marine Science and Technology, Qingdao, China. [4]Center for Monsoon System Research, Institute of Atmospheric Physics, Chinese Academy of Sciences, Beijing, China. [5]Key Laboratory of Earth System Numerical Modeling and Application, Institute of Atmospheric Physics, Chinese Academy of Sciences, Beijing, China. [6]CSIRO Environment, Hobart, TAS, Australia. [7]Earth System Numerical Simulation Science Center, Institute of Atmospheric Physics, Chinese Academy of Sciences, Beijing, China. ✉e-mail: tao@mail.iap.ac.cn; hg@mail.iap.ac.cn

to within 1.5 °C. Achieving this goal requires Carbon Dioxide Removal (CDR) methods to reduce atmospheric CO_2 concentrations[42–48]. Due to its large heat capacity, the ocean absorbs significant heat during the CO_2 ramp-up (RU) phase, and subsequently releases it during the ramp-down (RD) phase through slow oceanic dynamics, thereby influencing global climate[49–51]. This delayed response induces hysteresis and irreversibility in the global hydrological cycle under CDR scenarios[52–57]. Regional precipitation also exhibits asymmetric changes, such as in the tropical Pacific[56,58], East Asia[59], and South Asia[55,60]. While the direct response of global and regional precipitation to CDR is well-studied, the response of ENSO-driven tropical Pacific precipitation anomalies has received less attention. Understanding this response is crucial for projecting the variations of the WNPAC. A recent study indicates that ENSO SST variability shows hysteresis amplification under CDR scenarios, enhancing precipitation anomalies across the equatorial CEP and triggering stronger atmospheric teleconnections that intensify the WNPAC[61]. However, this investigation is based on a single model and does not fully address the dynamics driving the changes in precipitation anomalies across the equatorial CEP. Additionally, the effects of local precipitation anomalies in the tropical WNP on the anomalous anticyclone are not adequately considered.

Here, we utilize nine models from the Coupled Model Intercomparison Project Phase 6 (CMIP6) that conduct idealized CO_2 concentration experiments. These experiments involve a gradual increase in CO_2 concentrations from pre-industrial levels at a rate of 1% per year until reaching four times the pre-industrial concentrations over 140 years, followed by a symmetric decrease at the same rate for another 140 years, before stabilizing at the pre-industrial level for 60 years. Despite considerable spread in projection of ENSO SST variability, most models exhibit a strengthened response of precipitation anomalies to ENSO in the tropical WNP and equatorial CEP, as well as an enhancement of the WNPAC and its climate impacts during the El Niño mature winter when CO_2 concentrations return to pre-industrial levels.

Results

Asymmetric response of the WNPAC

The regressed SST anomalies, precipitation anomalies, and 850-hPa wind anomalies during D(0)JF(1) onto the standardized Niño-3.4 index during the CO_2 RU phase in multi-model ensemble (MME) are presented in Fig. 1a. In this research, the El Niño developing year is denoted as 0, and the subsequent El Niño decaying year is denoted as 1. Most models successfully reproduce the phase-locking feature of El Niño (Fig. S1a), which provides a reliable basis for further analyzing ENSO and its associated impacts. A notable feature is the hook-like pattern of positive precipitation anomalies across the equatorial CEP, while negative precipitation anomalies dominate the tropical WNP. As a combined contribution of direct Rossby wave response to the tropical WNP negative precipitation anomalies and remote forcing from the CEP positive precipitation anomalies[8], a fully developed anomalous anticyclone emerges in the WNP. Significant warm SST anomalies are observed in the equatorial CEP, and the tropical WNP region shows the cold SST anomalies, consistent with previous studies[8,21]. Most models accurately depict the observational characteristics of SST, precipitation, and wind anomalies during the El Niño mature winter, supported by consistency tests. However, compared to observations (Fig. S1b), the positive SST anomalies and precipitation anomalies in the equatorial Pacific extend too far westward, and there is a tendency to underestimate the positive precipitation anomalies in the equatorial central Pacific and the negative precipitation anomalies in the tropical WNP. Consequently, the simulated WNPAC appears relatively weaker (Fig. 1a and S1b).

To investigate whether the WNPAC exhibits an asymmetric response under the CDR scenario, we designate years from 230 to 280 in the CO_2 RD phase as the CO_2 RD period, and years from 1 to 51 in the CO_2 RU phase with consistent CO_2 concentrations as the CO_2 RU period. Figure 1b presents the differences in regressed variable fields between the two periods. The variations in SST anomalies across the equatorial CEP are not significant, indicating that the ENSO intensity remains relatively unchanged, resembling the patterns observed in global warming scenarios[62–67]. Compared to the SST anomalies, the positive precipitation anomalies in this region are considerably enhanced, suggesting a southeastward shift of the hook-like positive precipitation pattern, which likely influences the subsequent teleconnection impacts[32,63,65]. Over the WNP region, there is a significant intensification of the anomalous anticyclone, accompanied by enhanced local negative precipitation anomalies. The strengthened southwesterlies at northwest flank of WNPAC further exacerbate the warm temperature and positive precipitation anomalies in the East Asia-WNP region by hindering winter monsoon and transporting more warm and moist air to this area (Fig. S2b, S2d).

Further validation of the robustness of the WNPAC's asymmetric response under the CDR scenario is performed by calculating the WNPAC intensity throughout the entire phase of CO_2 concentrations change. The WNPAC intensity is defined using the area-weighted regional mean of the negative vorticity of the 850-hPa wind anomalies in the WNP region (0°–20°N, 100°–150°E, as indicated in Fig. 1a). This region well captures the anticyclonic circulation anomalies in each model (figure not shown). As depicted in Fig. 1c, the WNPAC gradually strengthens as CO_2 concentrations rise. During the CO_2 RD phase, due to the ocean's thermal inertia[49–51], the tropical climatological SST continues to increase for about 15 years, while the WNPAC continues to intensify for additional 25 years after CO_2 concentrations' peak. This overshoot and subsequent slow recovery lead to the WNPAC being stronger during the CO_2 RD period compared to the CO_2 RU period (Fig. 1b, c). Among the nine models, seven successfully capture the asymmetric characteristics of the WNPAC (Fig. S3). Additionally, an alternative definition by calculating the regionally averaged eddy geopotential height anomaly at 925-hPa following ref. 32 is applied to calculate the WNPAC intensity, yielding consistent results derived by the regional vorticity average (Fig. S4). To further validate the robustness of the asymmetric WNPAC response, horizontal distributions of 850-hPa wind and vorticity anomalies over the WNP region are presented, comparing the differences across nine pairs of periods. These periods span from years 1–51 (230–280) of the RU (RD) phase, with 10-year intervals, to years 81–131 (150–200) (Fig. S5). Consistency tests indicate that at least seven models simulate the anticyclonic circulation and negative vorticity anomalies in each time period.

Reasons for the asymmetric response of the WNPAC

The anomalous WNPAC is closely related to the local non-adiabatic cooling, which triggers the anomalous anticyclone as an Rossby wave response. Our findings demonstrate a remarkable concordance between precipitation anomalies in the tropical WNP and the WNPAC intensity (Fig. 1c), with correlation coefficients consistently exceeding the 90% confidence level in 8 models (Fig. S6). Similarly, equatorial CEP precipitation anomalies show a strong association with WNPAC intensity in the MME results (Fig. 1c), with that six models exhibit a significant correlation exceeding the 90% confidence level (Fig. S6). These equatorial CEP precipitation anomalies could influence tropical WNP precipitation anomalies through atmospheric teleconnections[8,21] or the Walker circulation[22,25–31], thereby affecting the strength of the anomalous anticyclone. While ENSO plays a significant role in influencing WNPAC, its SST variability does not seem to directly affect the intensity of the anticyclone. The correlation coefficients between ENSO SST variability and WNPAC in the nine modes are not significant, and only one models' results reach 90% confidence level (Fig. S7). Moreover, consistent with previous conclusion, the projection of ENSO SST variability across the nine models shows large spread. Therefore, our forthcoming investigation will focus on analyzing the origin of precipitation anomalies in the tropical WNP and equatorial CEP.

Predicted changes in ENSO-driven precipitation anomalies during the CO_2 RD relative to the RU period exhibit intensified negative anomalies in the tropical WNP and positive anomalies in the equatorial CEP (Figs. 1b and 2a). These precipitation anomalies are similar to those observed under global warming scenarios, as reported in previous studies[29–31,68–72]. Based on the two-layer approximated moisture budget equation[31], the

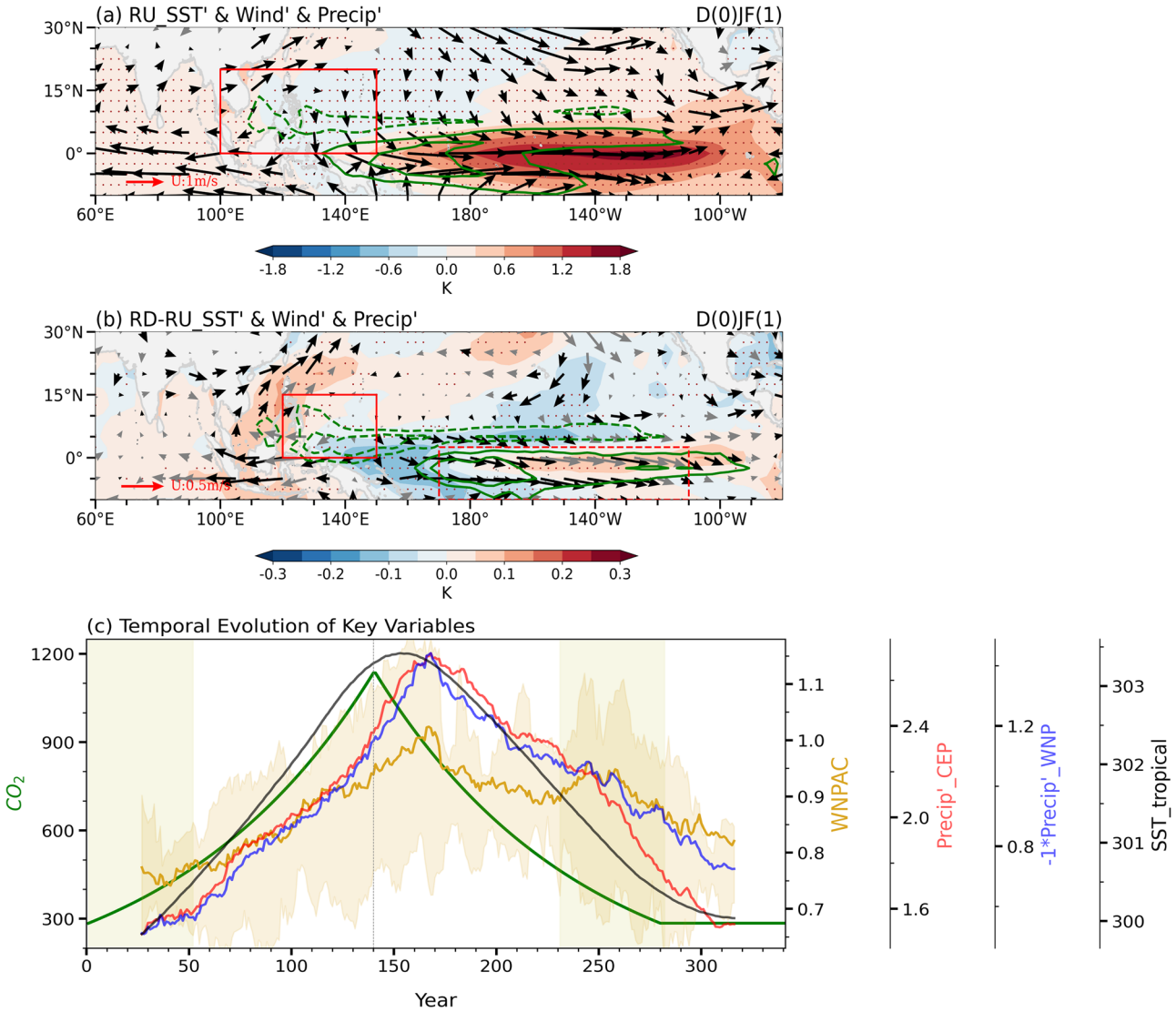

Fig. 1 | The asymmetric response of the WNPAC intensity. a Regressed SST anomalies (shading; unit: K), precipitation anomalies (contours; unit: mm day^{-1}) and 850-hPa wind anomalies (vectors; unit: m s^{-1}) during D(0)JF(1) onto the standardized Niño-3.4 index in the CO_2 RU period for 9 models' MME. Solid contours represent positive precipitation anomalies at 1.5 and 3.0 mm day^{-1}, while dashed contours denote negative anomalies at −1.5 and −3.0 mm day^{-1}. Red solid rectangles highlight the WNP (0°–20°N, 100°E–150°E) region. **b** Same as (**a**), but in the differences between the CO_2 RD and RU period. Solid contours represent positive precipitation anomalies at 0.5 and 1.0 mm day^{-1}, while dashed contours denote negative anomalies at −0.5 and −1.0 mm day^{-1}. Red solid and dashed rectangle respectively highlight the significant precipitation anomaly regions, specifically the tropical WNP (0°–15°N, 120°E–150°E) and the equatorial CEP (10°S–2.5°N, 170°E–110°W) regions. The black arrows and brown dots in (**a**, **b**) indicate consistency in results among at least 7 out of 9 models. **c** Evolution of CO_2 concentrations (unit: ppm), WNPAC intensity (unit: 10^{-6} s^{-1}), equatorial CEP region-averaged precipitation anomalies (red solid rectangle in Fig. 1b; unit: mm day^{-1}), tropical WNP region precipitation anomalies (red dashed rectangle in Fig. 1b; unit: mm day^{-1}), and tropical climatological SST (20°S–20°N, 180°W–180°E; unit: mm day^{-1}) for 9 models' MME. The yellow shading represents the intermodel spread, corresponding to the 3rd and 7th percentiles among the 9 models. The green shadings in (**c**) highlight the selected periods for CO_2 RU (1–51) and CO_2 RD (230–280). The prime symbols represent the anomalies caused by ENSO. The dashed vertical lines at year 140 in (**c**) mark the peak in CO_2 concentrations.

variation in precipitation anomalies ($\Delta P'$) can be decomposed into the thermodynamic ($-\Delta\bar{q}\cdot\omega'$) and dynamic ($-\bar{q}\cdot\Delta\omega'$) components. The simplified equation accurately captures the amplitude and spatial distribution of the changes in precipitation anomalies between the CO_2 RD and RU period (Fig. 2a, b). Compared to thermodynamic component ($-\Delta\bar{q}\cdot\omega'$), the dynamic component ($-\bar{q}\cdot\Delta\omega'$) plays a more dominant role (Fig. 2c, d). The dynamic component is largely controlled by the changes in vertical motion anomalies, confirmed by their resembling spatial distribution (Fig. 2d). Anomalous ascending and descending motions appear over the equatorial CEP and tropical WNP, respectively, indicating a further weakening of ENSO-induced anomalous Walker circulation during the CO_2 RD period. Given that circulation anomalies are primarily responsible for the precipitation anomalies, further analysis is necessary to determine the factors driving variations in vertical motion anomalies in the tropical WNP and equatorial CEP.

The intensified descending anomalies in the WNP

Due to data limitations, a simplified Moist Static Energy (MSE) equation for 5 models is used to analyze the intensified descending anomalies in the tropical WNP under the CDR scenario. As depicted in Fig. 3, the climatological MSE advection due to changes in anomalous vertical motion ($\langle\Delta\omega'\cdot\partial_p\bar{h}\rangle$) is primarily balanced by four factors: net MSE flux anomalies ($\Delta F'_{net}$), anomalous moist enthalpy advection due to changes in horizontal wind fields ($-\langle\Delta\vec{u}\cdot\nabla_h\bar{s}'\rangle$), anomalous horizontal advection of changed

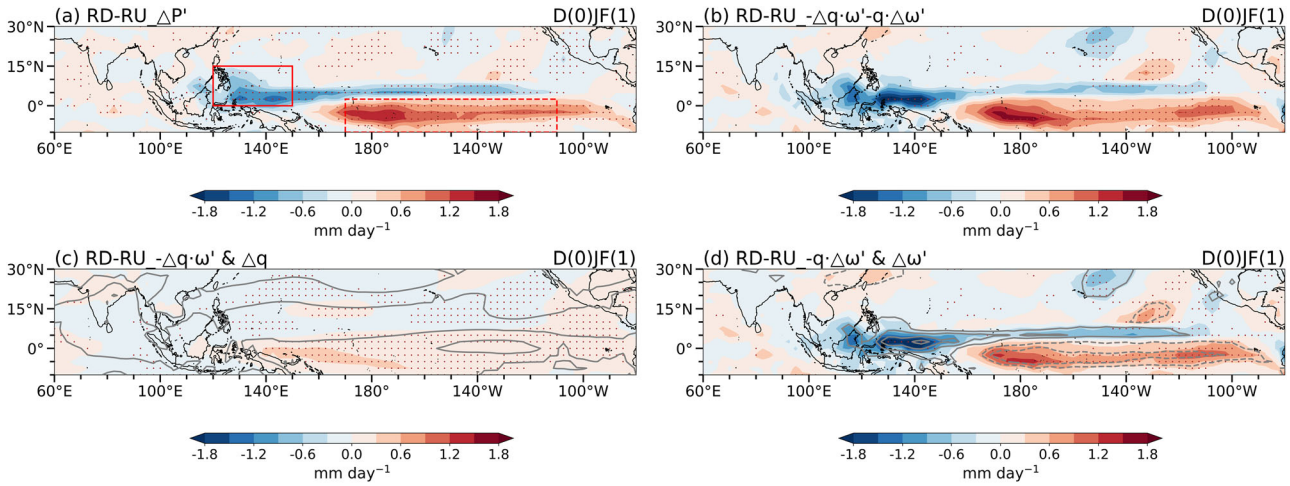

Fig. 2 | Tropical precipitation anomalies and moisture budget decomposition. **a** Regressed precipitation anomalies (shading; unit: mm day^{-1}) during D(0)JF(1) onto the standardized Niño-3.4 index in the differences between the CO_2 RD and RU period for 9 models' MME. Red solid and dashed rectangles respectively highlight the tropical WNP and the equatorial CEP region. **b** The combined effect of thermodynamic and dynamic term (shading; unit: mm day^{-1}) in the moisture budget decomposition in the differences between the CO_2 RD and RU period for 9 models' MME. **c** The effect of thermodynamic term (shading; unit: mm day^{-1}) and climatological surface specific humidity (contours; unit: g kg^{-1}) in the differences between the CO_2 RD and RU period for 9 models' MME. Solid contours represent positive climatological surface specific humidity with intervals of 0.3 g kg^{-1}. **d** The effect of dynamic term (shading; unit: mm day^{-1}) and vertical pressure velocity anomalies at 500-hPa (contours; unit: Pa day^{-1}) in the differences between the CO_2 RD and RU period for 9 models' MME. Solid contours represent positive vertical pressure velocity anomalies at 300, 600, 900, and 1200 pa day^{-1}, while dashed contours denote negative anomalies at −300, −600, −900 and −1200 pa day^{-1}. The brown dots indicate consistency in results among at least 7 out of 9 models. The prime symbols represent the anomalies caused by ENSO. The Δ symbols represent the deviation between the CO_2 RD and the RU period.

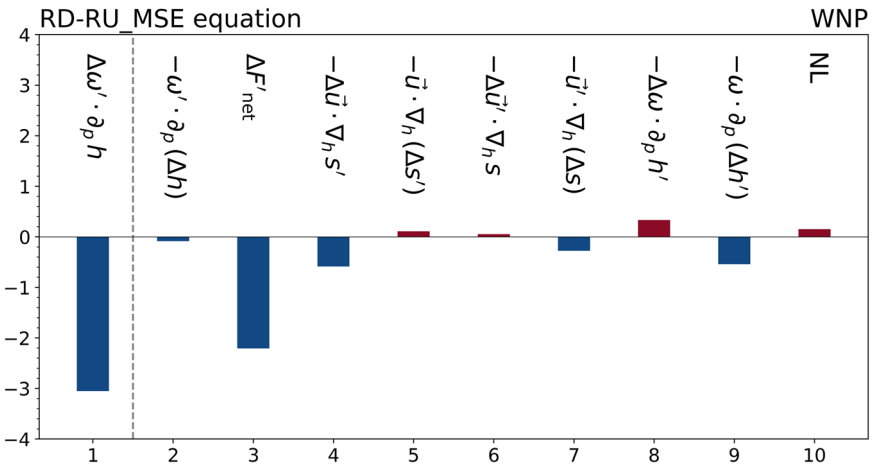

Fig. 3 | Budget analysis of the MSE (W m^{-2}) equation in the tropical WNP for 5 models' MME. The prime symbols represent the anomalies caused by ENSO. The Δ symbols represent the deviation between the CO_2 RD and the RU period.

climatological moist enthalpy ($-\langle\vec{u}' \cdot \nabla_h(\Delta\bar{s})\rangle$), and climatological vertical advection of the changed anomalous MSE ($-\langle\bar{\omega} \cdot \partial_p(\Delta h')\rangle$). The results for each model are shown in Fig. S8, with four of the five models successfully capturing the negative climatological MSE advection due to changes in anomalous vertical motion ($\langle\Delta\omega' \cdot \partial_p\bar{h}\rangle$), and the four important contributing factors in the MME generally exhibiting negative values in these four models. Figure S9 illustrates the spatial distribution of each term in MSE equation during the CO_2 RD compared to the RU period, and the above mentioned four terms exhibit negative anomalies in the tropical WNP (Fig. S9c, S9d, S9g, S9i), aligning with the effects of climatological MSE advection due to changes in anomalous vertical motion ($\langle\Delta\omega' \cdot \partial_p\bar{h}\rangle$; Fig. S9a). To further validate these terms, in addition to quantitatively analyzing the contribution of each term, their temporal evolution characteristics are provided in Fig. S10. The results reveal consistent overshoots and subsequent delayed recoveries in the four terms (Fig. S10c, S10d, S10g, S10i), indicating their crucial role in driving the enhanced descending anomalies in the region. These four terms involve different physical processes as external forcing and internal feedback mechanisms. The former drives variations in precipitation anomalies associated with changes of climatological background fields, while the latter amplifies the precipitation anomalies associated with changes of precipitation-related variable anomalies as feedback processes. The specific mechanisms are individually analyzed in following subsections.

External forcing. In the tropical WNP region, the vertical profile of anomalous moist enthalpy advection due to changes in horizontal wind fields ($-\langle\Delta\vec{u} \cdot \nabla_h s'\rangle$) indicates that the negative anomalies are primarily due to changes in the lower free troposphere (Fig. S11). Consequently, the spatial distribution of climatological winds and anomalous moist enthalpy at 700-hPa are selected for analysis. During the CO_2 RU period, the tropical WNP is characterized by climatological easterlies, and the distribution of anomalous moist enthalpy exhibits a maximum in the equatorial CEP (Fig. 4a), where corresponds to the significant SST warming (Fig. 1a). These climatological easterlies transport high

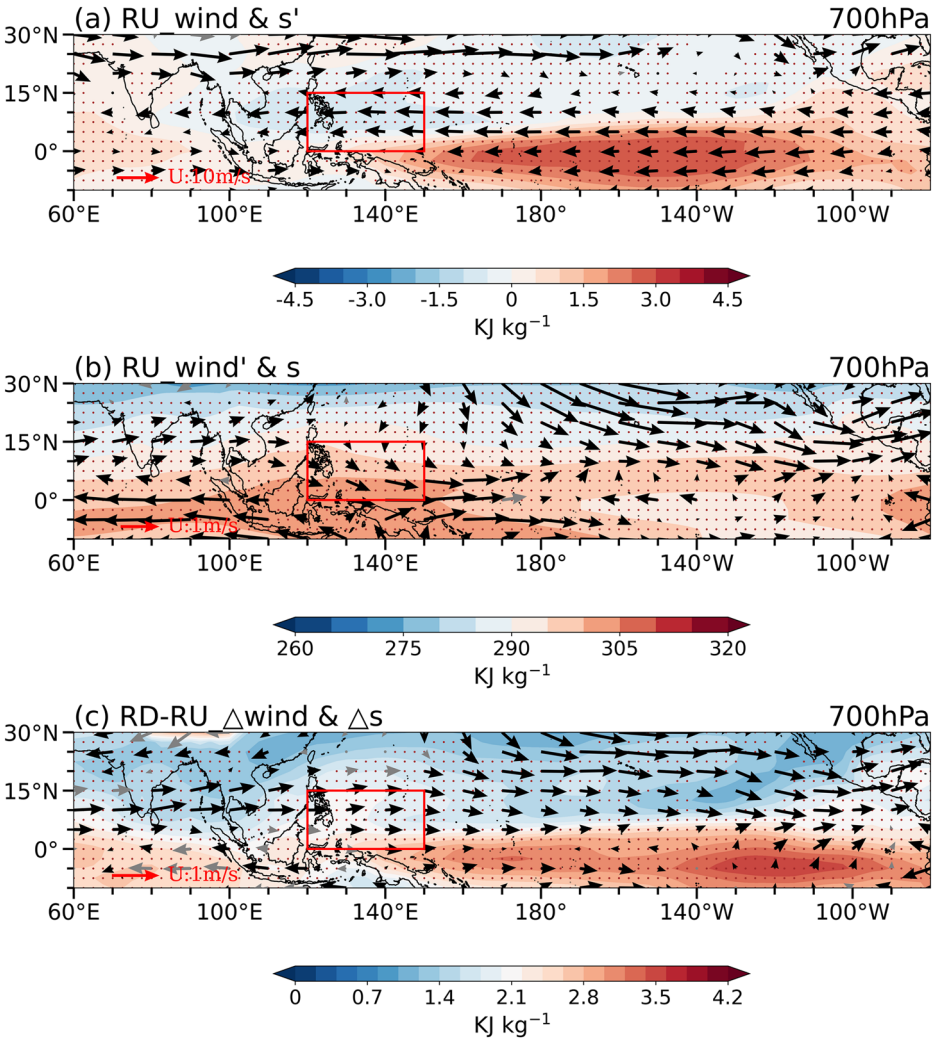

Fig. 4 | External forcing processes contributing to negative precipitation anomalies in the tropical WNP. a Climatological wind fields (arrows; unit: m s^{-1}) and regressed moist enthalpy anomalies (shading; kJ kg^{-1}) onto the standardized Niño-3.4 index at 700-hPa in the CO_2 RU period for 5 models' MME. **b** Same as (**a**), but wind anomalies (arrows; unit: m s^{-1}) and the climatological moist enthalpy (shading; kJ kg^{-1}). **c** Climatological wind fields (arrows; unit: m s^{-1}) and climatological moist enthalpy (shading; kJ kg^{-1}) at 700-hPa in the differences between the CO_2 RD and RU period for 5 models' MME. The black arrows and brown dots indicate consistency in results among at least 4 out of 5 models. Red solid rectangles highlight the tropical WNP region. The prime symbols represent the anomalies caused by ENSO. The Δ symbols represent the deviation between the CO_2 RD and the RU period.

anomalous enthalpy towards the tropical WNP, reducing the moist static stability of the atmospheric column and making this region more susceptible to convection.

During the CO_2 RD period, the climatological equatorial Pacific SST compared to CO_2 RU period presents an El Niño-like warming pattern[54,58–60], which enhances convective in the equatorial CEP following a warmer-get-wetter mechanism[58,73,74], corresponding with a convergence of climatological wind fields towards the equatorial CEP region (Fig. 4c). The resultant weakening of the climatological easterly winds in the tropical WNP reduces the transport of high anomalous moist enthalpy to the tropical WNP ($-\langle\Delta\vec{u}\cdot\nabla_h s'\rangle<0$), increasing the atmospheric moist static stability and thereby suppressing convection.

Interestingly, the vertical profile of anomalous horizontal advection of changed climatological moist enthalpy ($-\langle\vec{u}'\cdot\nabla_h(\Delta\bar{s})\rangle$) reveals that variations are also predominantly concentrated in the lower free troposphere (Fig. S12). Figure 4b illustrates the spatial distribution of anomalous wind fields and climatological moist enthalpy at 700-hPa during the CO_2 RU period. In El Niño mature winter, significant positive SST anomalies in the equatorial CEP (Fig. 1a) induce anomalous northwesterly winds over the tropical WNP. The climatological moist enthalpy is a function of climatological temperature and specific humidity. Although the temperature component accounts for 95.95% of total moist enthalpy in the tropical WNP, the analysis indicates that the anomalous horizontal advection of climatological moist enthalpy is predominantly contributed by the moisture advection, constituting 66.34% of the total effect (figure not shown). The climatological moist enthalpy in the tropical WNP exhibits a strong meridional gradient, and anomalous northerly winds bring low climatological moist enthalpy air to the region (Fig. 4b), stabilizing the atmospheric column and thus suppressing convection. This negative moist enthalpy advection is one of the key mechanisms for maintaining the wintertime WNPAC[21].

During the CO_2 RD period, significant increase of climatological moist enthalpy occurs in the equatorial Pacific (Fig. 4c), enhancing the meridional gradient of the climatological moist enthalpy. Thus, the resultant strengthened negative moist enthalpy advection ($-\langle\vec{u}'\cdot\nabla_h(\Delta\bar{s})\rangle<0$) over the tropical WNP corresponds to a further reduction of precipitation in this region. The decomposition of moist enthalpy indicates that the enhanced meridional gradient of changed climatological moist enthalpy is mainly due to changes in climatological specific humidity, while the contribution of temperature changes is minimal (Fig. S13a and S13b). The climatological equatorial Pacific warming pattern causes increased convections in the equatorial CEP and decreased convections along their north flank[58,75], as shown in Fig. S13c. These changes in convective activities induce changes in the climatological specific humidity through moisture-convection feedback mechanism[76,77], and the pattern correlation between them two reaches 0.68 for the region of 15°S to 15°N, and 60°E to 80°W (Fig. S13b and S13c).

Internal feedback. In the MSE budget analysis, the difference between the CO_2 RD and RU period shows that the net MSE flux anomalies ($\Delta F'_{net}$) play a dominant role in the enhanced descending anomalies over the tropical WNP (Fig. 3). As shown in Eq. (5), the net MSE flux anomalies ($\Delta F'_{net}$) includes five components, with longwave cloud

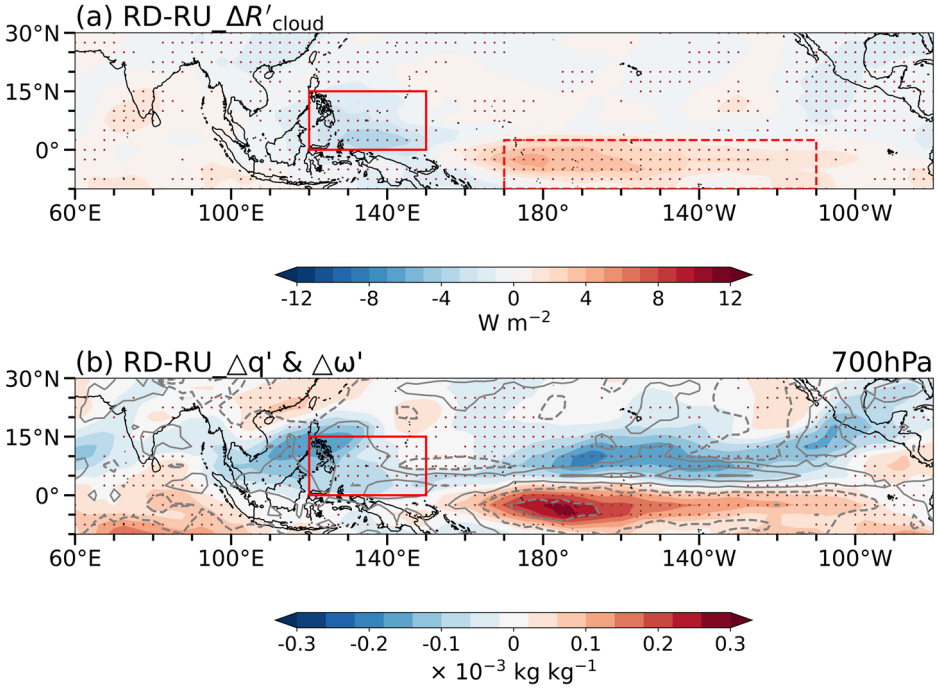

Fig. 5 | Internal feedback processes contributing to negative precipitation anomalies in the tropical WNP. a Regressed cloud-related longwave radiation into the atmospheric column (shading; unit: W m^{-2}) onto the standardized Niño-3.4 index in the differences between the CO_2 RD and RU period for 5 models' MME. **b** Regressed specific humidity anomalies (shading; unit: 10^{-3} kg kg^{-1}) and vertical pressure velocity anomalies (contours; unit: pa day^{-1}) at 700-hPa onto the standardized Niño-3.4 index in the differences between the CO_2 RD and RU period for 5 models' MME. Solid contours represent positive vertical pressure velocity anomalies at 100 and 400 pa day^{-1}, while dashed contours denote negative anomalies at −100 and −400 pa day^{-1}. The brown dots indicate consistency in results among at least 4 out of 5 models. Red solid and dashed rectangles respectively highlight the tropical WNP and the equatorial CEP region. The prime symbols represent the anomalies caused by ENSO. The Δ symbols represent the deviation between the CO_2 RD and the RU period.

radiative anomalies ($\Delta R'_{cloud}$) contributing the most significant change (Fig. 5a), accounting for 85.1% of changes in net MSE flux anomalies ($\Delta F'_{net}$). In contrast, the contributions of clear-sky longwave radiative, net solar radiative, latent heat flux, and sensible heat flux anomalies are about 18.8%, 0.2%, 7.3%, and 3.2%, respectively (figure not shown). The cloud-related net longwave radiative flux anomalies (R'_{cloud}) in the tropics reflect an internal positive feedback between atmospheric convection and cloud radiative forcing[78–81], as that pattern correlation between them in the tropical region of 15°S to 15°N, and 60°E to 80°W reaches 0.83 (Figs. 2d and 5a). In the tropical WNP, the further suppression of convection leads to an additional decrease in negative longwave cloud radiative anomalies ($\Delta R'_{cloud}$), which cool atmospheric column, enhance gross moisture stability, and thereby further inhibit convection[21]. This convection-cloud radiative positive feedback amplifies the negative precipitation anomalies but is not the root cause of it.

In addition to the convection-cloud radiative feedback, there exists another positive feedback mechanism that contributes to the negative precipitation anomalies in this region. During the RU period, the minimum MSE anomalies in the tropical WNP appears around 700-hPa (Fig. S14a), indicating an increase in the gross moist stability of the atmospheric column in the climatological deep convection region ($-\langle\bar{\omega}\cdot\partial_p h'\rangle<0$). The vertical structure of these MSE anomalies is primarily controlled by specific humidity anomalies, while the contribution of dry static energy anomalies is relatively minor (figure not shown). Furthermore, this vertical distribution of specific humidity anomalies is related to moisture-convection feedback, and large-scale descending anomalies in the tropical WNP lead to a reduction in mid-to-lower free atmospheric level moisture anomalies, as explained by ref. 21.

During the CO_2 RD period, the vertical profile of MSE anomalies shows a further reduction around 700-hPa compared to the CO_2 RU period (Fig. S14b), mainly due to changes in specific humidity anomalies (Fig. S14d). The pattern correlation between these specific humidity anomalies and vertical pressure velocity anomalies at 700-hPa in the tropical region of 15°S to 15°N, 60°E to 80°W is approximately 0.67 (Fig. 5b), suggesting an important role for moisture-convection positive feedback. In the tropical WNP, enhanced descending anomalies further reduce specific humidity anomalies (Fig. 5b), resulting in reduced climatological upward advection of the anomalous MSE ($-\langle\bar{\omega}\cdot\partial_p(\Delta h')\rangle<0$) and increased gross moisture stability of the atmospheric column, thereby suppressing convection. Additionally, there is some enhancement of MSE anomalies at the top of the free troposphere, related to changes in atmospheric temperature anomalies (Fig. S14c), which to some extent reduces the vertical gradient of MSE anomalies. These changes in atmospheric temperature anomalies are associated with the moist adiabatic adjustment of tropical convection, meaning that when specific humidity anomalies are confined to the lower free troposphere, atmospheric temperature anomalies in the upper free troposphere increase correspondingly to maintain tropical moist adiabats[5,82,83].

The intensified ascending anomalies in the CEP

The MSE equation for 5 models is also utilized to explore the enhanced ascending anomalous over the equatorial CEP under CDR scenario (Fig. 6). The climatological MSE advection due to changes in anomalous vertical motion ($\langle\Delta\omega'\cdot\partial_p\bar{h}\rangle$) is primarily balanced by anomalous vertical advection of the changed climatological MSE ($-\langle\omega'\cdot\partial_p(\Delta\bar{h})\rangle$), net MSE flux anomalies ($\Delta F'_{net}$), climatological moist enthalpy advection due to changes in anomalous horizontal winds ($-\langle\Delta\vec{u}'\cdot\nabla_h\bar{s}\rangle$), and anomalous MSE advection due to changes in climatological vertical motion ($-\langle\Delta\bar{\omega}\cdot\partial_p h'\rangle$). Figure S15 provides the results for each model, showing that all five models successfully capture the positive climatological MSE advection due to changes in anomalous vertical motion ($\langle\Delta\omega'\cdot\partial_p\bar{h}\rangle$), with the four key contributing factors in the MME generally exhibiting positive values across these models. The spatial distribution of these four terms exhibit positive anomalies over the equatorial CEP during the CO_2 RD relative to the RU period (Fig. S9b, S9c, S9f, S9h), and their temporal evolution aligns with the climatological MSE advection due to changes in anomalous vertical motion ($\langle\Delta\omega'\cdot\partial_p\bar{h}\rangle$; Fig. S16a, S16b, S16c, S16f, S16h), exhibiting characteristics of overshoot and delayed recovery and indicating their contribution to the strengthened positive precipitation anomalies over the equatorial CEP. The corresponding physical processes of these four terms from the perspectives of external forcing and internal feedback processes are examined in the next subsections.

External forcing. During the CO_2 RU period, the climatological MSE in the equatorial CEP reaches its lowest value at approximately 700-hPa, cooperating with the ascending anomalies in the lower to mid

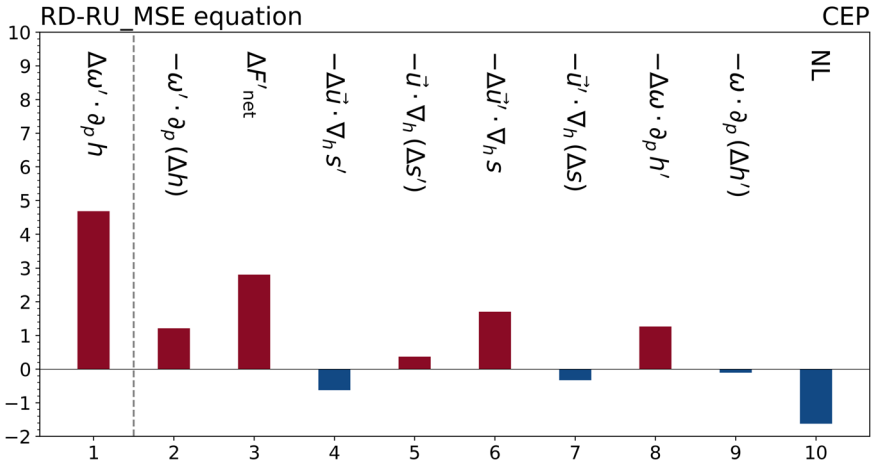

Fig. 6 | Same as Fig.3, but in the equatorial CEP.

troposphere to enhance the gross moist stability of the atmospheric column ($-\langle\omega' \cdot \partial_p \bar{h}\rangle < 0$, Fig. 7a). The difference between the CO_2 RD and RU period indicates that the increase in climatological MSE over the equatorial CEP is most pronounced in the lower troposphere (Fig. 7a) and is associated with climatological equatorial Pacific warming pattern.

The equatorial CEP SST warming, on one hand, favors a direct increase in boundary layer moisture, on the other hand, enhances convection in the area[58,75] and thereby increases lower troposphere moisture (Fig. S17c) through the moisture-convection feedback process[76,77]. The strengthened climatological moisture primarily contributes to the increase of climatological MSE in the lower free troposphere (Fig. 7a), which aligns with anomalous ascending motion to weaken atmospheric gross moist stability ($-\langle\omega' \cdot \partial_p(\Delta\bar{h})\rangle > 0$) and thereby promotes convection. Ref. 84 also demonstrates that this term is the main contributor to the enhanced precipitation over the equatorial CEP under global warming scenario. Additionally, the equatorial CEP SST warming leads to changes in climatological atmospheric temperature through moist-adiabatic adjustment (Fig. S17b), resulting in a weak positive center of climatological MSE at around 250-hPa (Fig. 7a). This weak positive center reduces the vertical gradient of the changed climatological MSE and inhibits enhanced convection to some extent.

Moreover, anomalous MSE advection due to changes in climatological vertical motion ($-\langle\Delta\bar{\omega} \cdot \partial_p h'\rangle$) also contributes to the enhancement of precipitation anomalies. The equatorial western Pacific is a region of deep convection dominated by strong climatological ascending motions, whereas the equatorial eastern Pacific, being the descending branch of the Walker circulation, experiences climatological descending motions (Fig. 7b). Simultaneously, the vertical distribution of MSE anomalies across the entire equatorial Pacific shows a decrease from the lower to the upper free troposphere (Fig. S17e). Consequently, in the equatorial eastern Pacific, anomalous MSE transported by descending motions enhance gross moist stability ($-\langle\bar{\omega} \cdot \partial_p h'\rangle < 0$) and suppresses convection.

During the CO_2 RD period, the climatological equatorial Pacific warming pattern shift the Walker circulation eastward, characterized by enhanced ascending motions in the equatorial CEP and stronger descending motions in the western Pacific (Fig. 7b; ref. 59), consistent with the conclusions under global warming scenario[28,29,85]. The anomalous MSE transported by enhanced ascending motions reduce the gross moist stability of the region ($-\langle\Delta\bar{\omega} \cdot \partial_p h'\rangle > 0$) and facilitate enhanced convection.

Internal feedback. Similar to the conclusions for the tropical WNP, net radiative flux anomalies ($\Delta F'_{net}$) contribute the most to the enhanced ascending anomalies over the equatorial CEP according to MSE budget analysis (Fig. 6). Among the five components included in the simplified net MSE flux anomalies ($\Delta F'_{net}$), changes in longwave cloud radiative forcing anomalies ($\Delta R'_{cloud}$) are the most significant, accounting for 58.2% of changes in net MSE flux anomalies ($\Delta F'_{net}$). Contributions from changes in clear-sky longwave radiative, net solar radiative, latent heat, and sensible heat flux anomalies are approximately 13.1%, 3.7%, 19.3%, and 5.7%, respectively (figure not shown). In contrast to the tropical WNP, the further enhancement of convection in the equatorial CEP leads to an additional increase in positive longwave cloud radiative anomalies ($\Delta R'_{cloud}$), which warm atmospheric column, reduce gross moisture stability, and thereby further promote convection as a convection-cloud radiative positive feedback (Fig. 5a).

Another internal feedback process is related to climatological moist enthalpy advection due to changes in anomalous horizontal winds ($-\langle\Delta\vec{u}' \cdot \nabla_h\bar{s}\rangle$), with its positive changes primarily concentrated in the tropopause and lower free troposphere (Fig. S18). Therefore, 100-hPa and 700-hPa are selected for detailed analysis. At 100-hPa, climatological moist enthalpy is predominantly influenced by atmospheric temperature due to the very low water vapor content at the level, and it increases from west to east across the equatorial Pacific (Fig. 8a). The low-value center of climatological moist enthalpy in the equatorial western Pacific is caused by the adiabatic cooling effect of climatological ascending airflows (Fig. 7b). At 700-hPa, climatological moist enthalpy is affected by both atmospheric temperature and moisture, showing a decrease from west to east across the equatorial Pacific (Fig. 8b), owing to that the high climatological moist enthalpy is close to the warm pool in the equatorial western Pacific.

During the CO_2 RU period, the vertical cross-sections of the equatorial wind fields reveal pronounced anomalous ascending (descending) motions in the equatorial CEP (western Pacific) in response to El Niño, corresponding with anomalous easterlies (westerlies) at upper (lower) troposphere (Fig. S19a). During the CO_2 RD period, the enhanced equatorial CEP convection anomalies further strengthen upper-level easterly wind anomalies (Figs. 8a and S19b) and lower-level westerly wind anomalies (Figs. 8b and S19b), both of which bring more high climatological moist enthalpy air to the equatorial CEP ($-\langle\Delta\vec{u}' \cdot \nabla_h\bar{s}\rangle > 0$) and promote convection. Previous study has used this wind-enthalpy-convection positive feedback to explain the formation of negative precipitation anomalies in the tropical WNP and the subsidence anomalies in the northern flank of the equatorial Pacific[21,79].

Discussion

This study investigates the irreversible response of the anomalous WNPAC and its climate impacts during the El Niño mature winter to CO_2 forcing, as well as the underlying physical mechanisms. The results reveal that the WNPAC progressively strengthens with increasing CO_2 concentrations, reaching its maximum intensity in the first few decades of CO_2 RD phase before gradually weakening. However, the anticyclone does not fully return to its initial state even when the CO_2 concentrations are reduced to the pre-industrial level.

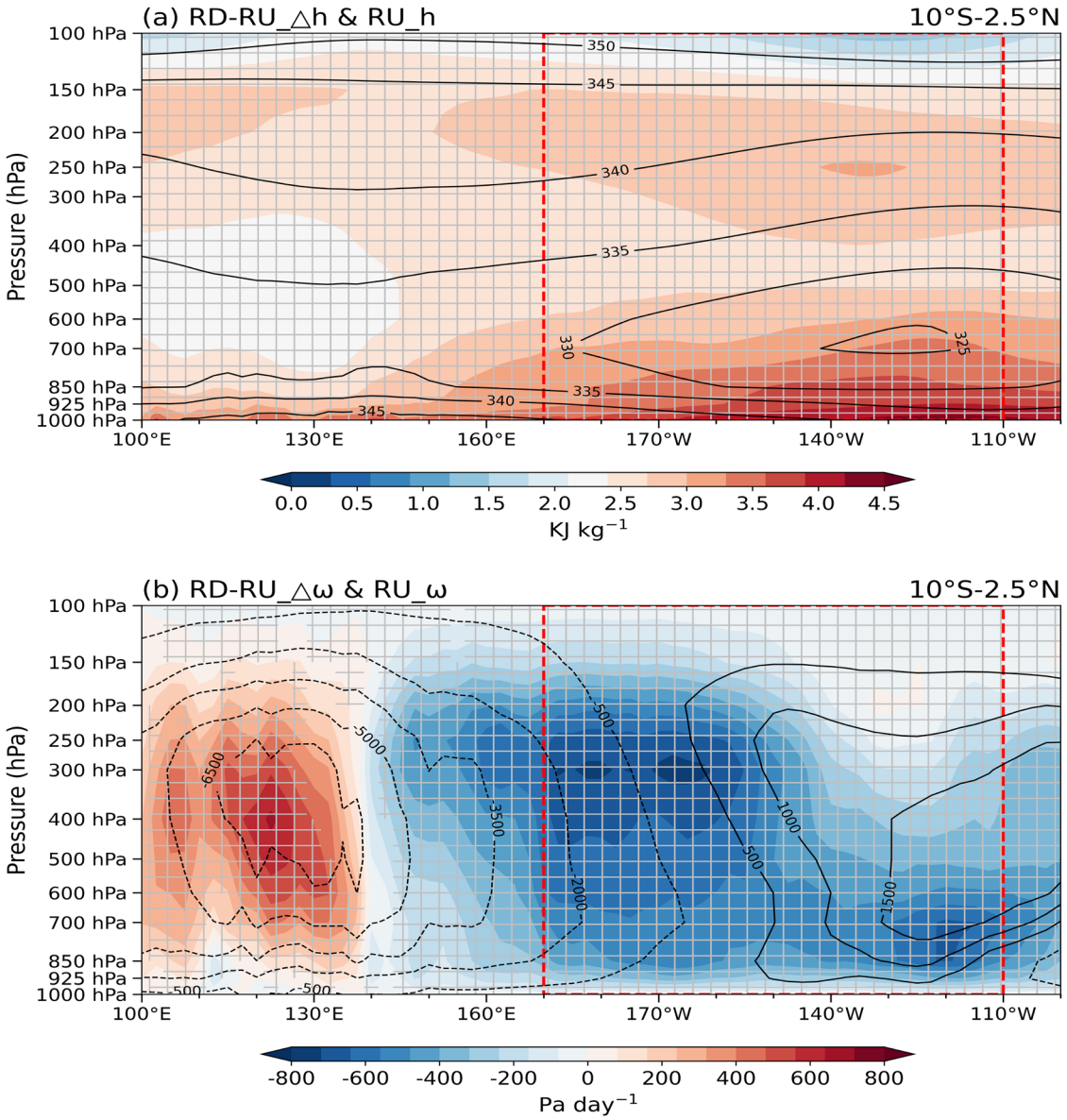

Fig. 7 | External forcing processes contributing to positive precipitation anomalies in the equatorial CEP. a Meridional average (10°S–2.5°N) of climatological MSE in the CO_2 RU period (contours; unit: KJ kg^{-1}) and in the differences between the CO_2 RD and RU period (shading; unit: KJ kg^{-1}) for 5 models' MME. **b** Same as (**a**), but the climatological vertical pressure velocity in the CO_2 RU period (contours; unit: pa day^{-1}) and in the differences between the CO_2 RD and RU period (shading; unit: pa day^{-1}). The gray grids indicate consistency in results among at least 4 out of 5 models. Red dashed rectangles highlight the equatorial CEP region. The Δ symbols represent the deviation between the CO_2 RD and the RU period.

This overshoot and the subsequent slow recovery of the anomalous WNPAC are primarily due to the enhanced negative precipitation anomalies in the tropical WNP as a Rossby wave response, and further promoted by the enhanced positive precipitation anomalies in the equatorial CEP through the adjustments of atmospheric teleconnections and Walker circulation. These changed precipitation anomalies are mainly driven by variations in vertical motion anomalies. The key processes and mechanisms are summarized in a schematic diagram and explained as follows (Fig. 9).

In the tropical WNP, the enhanced negative precipitation anomalies are driven by remote forcing from the equatorial CEP, and subsequently amplified by local feedback processes. The climatological equatorial Pacific El Niño-like warming pattern weakens the climatological easterlies and increases the meridional gradient of climatological specific humidity in the lower free troposphere of the tropical WNP. These changes reduce the horizontal transport of high anomalous moist enthalpy by the climatological easterlies ($-\langle \Delta\bar{\vec{u}} \cdot \nabla_h s' \rangle < 0$) and enhance the horizontal transport of low climatological moist enthalpy by the anomalous northerlies ($-\langle \vec{u}' \cdot \nabla_h(\Delta\bar{s}) \rangle < 0$), thereby suppressing convection. The suppressed convection, through convection-cloud radiative feedback, reduces the cloud's reflection of longwave radiation, leading to a net MSE flux outflow of atmosphere ($\Delta F'_{net} < 0$). Additionally, suppressed convection reduces specific humidity anomalies in the lower troposphere through moisture-convection feedback processes, reducing the upward transport of anomalous MSE ($-\langle \bar{\omega} \cdot \partial_p(\Delta h') \rangle < 0$). These two internal feedback processes enhance the gross moist stability of atmospheric column, further amplifying negative precipitation anomalies.

In the equatorial CEP, climatological equatorial Pacific warming pattern increases the lower free troposphere climatological MSE and climatological precipitation, strengthening upward transport of climatological MSE ($-\langle \omega' \cdot \partial_p(\Delta\bar{h}) \rangle > 0$) and anomalous MSE ($-\langle \Delta\bar{\omega} \cdot \partial_p h' \rangle > 0$). Both processes weaken atmospheric gross moist

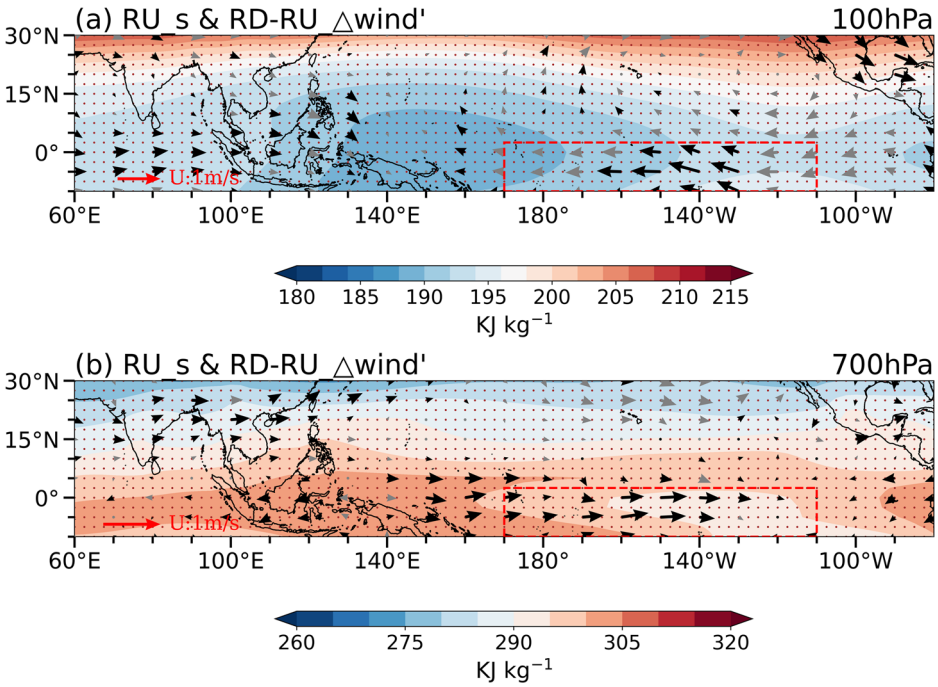

Fig. 8 | Internal feedback processes contributing to positive precipitation anomalies in the equatorial CEP. a Climatological moist enthalpy (shading; unit: KJ kg^{-1}) in the CO_2 RU period and regressed wind fields (arrows; unit: m s^{-1}) onto the standardized Niño-3.4 index in the differences between the CO_2 RD and RU period at 100-hPa for 5 models' MME. **b** Same as (**a**), but at 700-hPa. The black arrows and brown dots indicate consistency in results among at least 4 out of 5 models. Red dashed rectangles highlight the equatorial CEP region. The prime symbols represent the anomalies caused by ENSO. The Δ symbols represent the deviation between the CO_2 RD and the RU period.

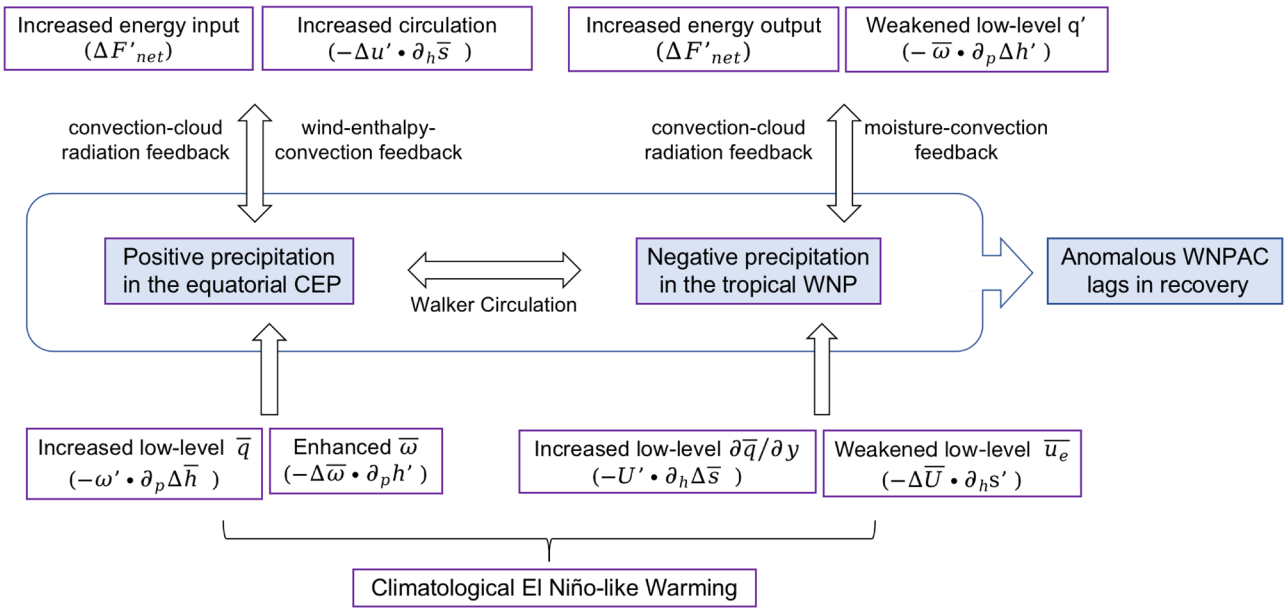

Fig. 9 | Key processes involved in the asymmetric response of the anomalous WNPAC intensity during El Niño mature winter.

stability and enhance convection in the region. The enhanced convective anomalies, on one hand, strengthen the input of net radiative flux anomalies ($\Delta F'_{net} > 0$) to atmosphere through convection-cloud radiation feedback, and on the other hand, drive the low-level horizontal convergent winds and the upper-level horizontal divergent winds, thereby transporting more high climatological moist enthalpy air to the region ($-\langle \Delta\vec{u}' \cdot \nabla_h \bar{s} \rangle > 0$). This wind-enthalpy-convection feedback further intensifies the convective anomalies.

Under the CDR scenarios, climatological equatorial Pacific warming pattern is primarily associated with deep ocean warming[54,59], which is due to the immense heat capacity and slow ocean dynamical processes[49–51]. The gradual recovery of the Walker circulation plays a mutually reinforcing role in this warming pattern. This type of warming causes the significant southward shift of the intertropical convergence zone[75], and the increase in climatological humidity is particularly evident over the CEP, indicating its southeastward movement (Fig. 2c). The changes in precipitation anomalies in the equatorial CEP and tropical WNP also exhibit a southeastward shift (Fig. 1b). However, the relationship between positional shift of climatological humidity and precipitation anomalies, and the corresponding low-level circulation response, particularly the positional changes of the WNPAC, are not fully discussed in the present study and require further research, as it could impact the spatial distribution of climate anomalies in East Asia-WNP (Fig. S2b).

Methods

The idealized CDR pathway

This study utilizes data from the CMIP6 1pctCO2 and 1pctCO2-cdr experiments. In the 1pctCO2 experiment, CO_2 concentrations increase annually by 1% over 150 years from the pre-industrial levels of 284.7 ppm, quadrupling by year 140 to reach 1138.8 ppm. The 1pctCO2-cdr experiment features symmetric CO_2 removal over 140 years, followed by stabilization at the pre-industrial levels for at least 60 additional years. We use data from the first 140 years of the 1pctCO2 experiment and the first 200 years of the 1pctCO2-cdr experiment to construct idealized CO_2 RU and RD scenarios. In this scenario, CO_2 concentrations rise from year 1 to year 140, decline symmetrically from year 141 to year 280, and stabilize from year 281 to year 340.

Data preprocessing

The experiments involve an ensemble of nine climate models: ACCESS-ESM1-5, CanESM5, CAS-ESM2-0, CESM2, CNRM-ESM2-1, GFDL-ESM4, MIROC-ES2L, NorESM1-LM, and UKESM1-0-LL. All model datasets are initially interpolated onto a standardized 2.5° × 2.5° grid to ensure consistency. To extract interannual signals and assess variables' responses to ENSO, an 8-year high-pass filter is applied, removing trends and interdecadal signals. Subsequently, interannual anomalies are calculated by subtracting the climatological mean for the entire study period. These anomalies are then regressed against the standardized Niño-3.4 index [SST anomalies averaged over 5°S–5°N, 120°–170°W during D(0)JF(1)]. This regression used a 51-year moving window for each model individually, and the results were averaged to create MME, thus minimizing biases from any single model.

Monthly outputs from all nine models are to examine the asymmetric response of the WNPAC and associated precipitation anomalies. However, CAS-ESM2-0, CESM2, NorESM2-LM, and UKESM1-0-LL are excluded from the MSE budget analysis due to data limitations. Consequently, only five models were used to study the mechanisms driving asymmetric vertical motion anomalies in the tropical WNP and equatorial CEP. In this study, a significant consensus among the models is identified as being present if at least 70% of the models agreed on the sign of the anomalies[86]. Specifically, for cases with 9 models, this threshold corresponds to an agreement among at least 7 models, while for cases with 5 models, an agreement among at least 4 models is required. Correlation analysis is used, and the confidence level is estimated based on the standard two-tailed Student's t test. The effective degrees of freedom are considered when applying the t test. The effective degrees of freedom (N_{eff}) is estimated using the formula $N_{eff} = N \cdot (1 - r_1 \cdot r_2)/(1 + r_1 \cdot r_2)$, where N is the sample size, and r_1 and r_2 are the lag-1 autocorrelation coefficients of the time series[87].

The observational and reanalysis datasets employed in this study are as follows: (1) the Hadley Centre Global Sea Surface Temperature (HadISST) dataset, (2) the Global Precipitation Climatology Project (GPCP) monthly precipitation dataset, and (3) the National Centers for Environmental Prediction-Department of Energy (NCEP-DOE) reanalysis. All these datasets span the period from 1981 to 2010 and are interpolated and processed in a manner consistent with the CMIP6 model outputs.

Moisture budget decomposition

The decomposition of the moisture budget simplifies the understanding of rainfall changes by separating thermodynamic and dynamic components. This approach effectively delineates the spatial patterns of tropical precipitation alterations under both warming and CDR scenarios, as well as elucidates the interactions between precipitation and atmospheric circulation[31,58,60,72]. The equation used to describe the ENSO-induced rainfall changes is presented as follows:

$$\Delta P' \sim -\left(\Delta\bar{q} \cdot \omega' + \bar{q} \cdot \Delta\omega'\right) \tag{1}$$

In this formulation, Δ signifies the changes observed during the CO_2 RD period relative to the CO_2 RU period. The prime symbol indicates anomalies attributable to ENSO, and the overbar represents the climatological mean. The variables P, q, and ω correspond to precipitation, surface specific humidity, and 500-hPa vertical pressure velocity [negative (positive) ω indicates upward (downward) motion], respectively. The term $\Delta\bar{q} \cdot \omega'$ is regarded as the thermodynamic component associated with climatological moisture, while $\bar{q} \cdot \Delta\omega'$ is considered as the dynamic component related to circulation anomalies.

MSE budget

In the tropics, vertical motion is primarily regulated by the MSE budget[88]. The MSE equation is expressed as:

$$\partial_t\langle s\rangle' + \langle\vec{u} \cdot \nabla_h s\rangle' + \langle\omega \cdot \partial_p h\rangle' = F'_{net} \tag{2}$$

Here, MSE is defined as $h = c_pT + L_vq + gz$, where $s = c_pT + L_vq$ represents moist enthalpy. The terms $\vec{u}$, ω, q, T, and z, and F_{net} correspond to horizontal wind, vertical pressure velocity, specific humidity, atmospheric temperature, and geopotential height, respectively, while F_{net} denote the net MSE flux. The constants c_p, L_v, and g represent the specific heat at constant pressure, latent heat of vaporization, and acceleration due to gravity, respectively. It is noted that the time tendency term $\partial_t\langle s\rangle'$ is negligible on interannual timescales. According to ref. 84, variations in the MSE equation between CO_2 RD and CO_2 RU period can be reformulated as:

$$\begin{aligned}\langle\Delta\omega' \cdot \partial_p\bar{h}\rangle \approx &-\langle\omega' \cdot \partial_p\left(\Delta\bar{h}\right)\rangle + \Delta F'_{net}\\ &-\langle\Delta\vec{\bar{u}} \cdot \nabla_h s'\rangle - \langle\Delta\vec{\bar{u}} \cdot \nabla_h(\Delta s')\rangle\\ &-\langle\Delta\vec{u}' \cdot \nabla_h\bar{s}\rangle - \langle\vec{u}' \cdot \nabla_h(\Delta\bar{s})\rangle\\ &-\langle\Delta\bar{\omega} \cdot \partial_p h'\rangle - \langle\bar{\omega} \cdot \partial_p\left(\Delta h'\right)\rangle + NL,\end{aligned} \tag{3}$$

where NL indicates the sum of all nonlinear terms. The net MSE flux, F'_{net}, entering an atmospheric column includes components from both the top and the surface of the atmosphere:

$$F'_{net} = \left(S_t^{\downarrow} - S_t^{\uparrow} - R_t^{\uparrow}\right) - \left(-S_s^{\uparrow} + S_s^{\downarrow} - R_s^{\uparrow} + R_s^{\downarrow} - LH - SH\right) \tag{4}$$

The first three terms ($S_t^{\downarrow}$, $S_t^{\uparrow}$, $R_t^{\uparrow}$) represent radiative fluxes entering an atmospheric column from the top of the atmosphere, including downward shortwave, upward shortwave, and upward longwave radiative fluxes. Conversely, the subsequent six terms ($S_s^{\uparrow}$, $S_s^{\downarrow}$, $R_s^{\uparrow}$, $R_s^{\downarrow}$, LH, SH) describe fluxes entering from the surface, which encompass both shortwave and longwave radiative fluxes in both directions, along with latent and sensible heat fluxes. Positive values in this context denote heating of the atmosphere.

The three longwave radiation terms ($R_t^{\uparrow}$, $R_s^{\uparrow}$, $R_s^{\downarrow}$) are consolidated and termed as net longwave radiation flux (R'_{net}), which are further subdivided into cloud-related (R'_{cloud}) and clear-sky (R'_{clear}) components. Similarly, the four solar radiation terms ($S_t^{\downarrow}$, $S_t^{\uparrow}$, $S_s^{\uparrow}$, $S_s^{\downarrow}$) are amalgamated and referred to as net solar radiation flux (S'_{net})[21]. Thus, the net MSE flux differences between CO_2 RD and CO_2 RU period are captured by:

$$\Delta F'_{net} = \Delta R'_{cloud} + \Delta R'_{clear} + \Delta S'_{net} + \Delta LH' + \Delta SH' \tag{5}$$

Data availability

The CMIP6 outputs are publicly available online at https://esgf-node.llnl.gov/projects/cmip6/. The observational and reanalysis data used to evaluate the performance of the models in this study can be accessed from the following sources: the HadISST dataset at https://www.metoffice.gov.uk/hadobs/hadisst/data/download.html, the GPCP dataset at https://psl.noaa.gov/data/gridded/data.gpcp.html, and the NCEP-DOE reanalysis dataset at https://psl.noaa.gov/data/gridded/data.ncep.reanalysis2.pressure.html.

Received: 27 August 2024; Accepted: 26 November 2024;
Published online: 05 December 2024

References

1. Trenberth, K. E., Caron, J. M., Stepaniak, D. P. & Worley, S. Evolution of El Niño-Southern oscillation and global atmospheric surface temperatures. *J. Geophys. Res. Atmos.* **107**, AAC 5-1–AAC 5-17 (2002).
2. McPhaden, M. J., Zebiak, S. E. & Glantz, M. H. ENSO as an integrating concept in earth science. *Science* **314**, 1740–1745 (2006).
3. Deser, C., Alexander, M. A., Xie, S.-P. & Phillips, A. S. Sea surface temperature variability: patterns and mechanisms. *Annu. Rev. Mar. Sci.* **2**, 115–143 (2010).
4. Tao, W. et al. Asymmetry in summertime atmospheric circulation anomalies over the northwest Pacific during decaying phase of El Niño and La Niña. *Clim. Dyn.* **49**, 2007–2023 (2017).
5. Hu, K., Huang, G., Huang, P., Kosaka, Y. & Xie, S.-P. Intensification of El Niño-induced atmospheric anomalies under greenhouse warming. *Nat. Geosci.* **14**, 377–382 (2021).
6. Wang, Y., Hu, K., Huang, G. & Tao, W. Asymmetric impacts of El Niño and La Niña on the Pacific-North American teleconnection pattern: the role of subtropical jet stream. *Environ. Res. Lett.* **16**, 114040 (2021).
7. Wang, Y., Hu, K., Huang, G. & Tao, W. The role of nonlinear energy advection in forming asymmetric structure of ENSO teleconnections over the North Pacific and North America. *Geophys. Res. Lett.* **50**, e2023GL105277 (2023).
8. Wang, B., Wu, R. & Fu, X. Pacific-East Asian teleconnection: How does ENSO affect East Asian climate? *J. Clim.* **13**, 1517–1536 (2000).
9. Wang, B., Wu, R. & Li, T. Atmosphere-warm ocean interaction and its impacts on Asian-Australian monsoon variation. *J. Clim.* **16**, 1195–1211 (2003).
10. Wu, R., Hu, Z.-Z. & Kirtman, B. P. Evolution of ENSO-related rainfall anomalies in East Asia. *J. Clim.* **16**, 3742–3758 (2003).
11. Chou, C. Establishment of the low-level wind anomalies over the western North Pacific during ENSO development. *J. Clim.* **17**, 2195–2212 (2004).
12. Xie, S.-P. et al. Indian Ocean capacitor effect on Indo-western Pacific climate during the summer following El Niño. *J. Clim.* **22**, 730–747 (2009).
13. Tao, W. et al. Origins of biases in CMIP5 models simulating northwest Pacific summertime atmospheric circulation anomalies during the decaying phase of ENSO. *J. Clim.* **31**, 5707–5729 (2018).
14. Zhang, R.-H., Sumi, A. & Kimoto, M. Impact of El Niño on the East Asian monsoon: a diagnostic study ofthe '86/87 and '91/92 events. *J. Meteorol. Soc. Jpn. Ser. II* **74**, 49–62 (1996).
15. Gong, H. et al. Diverse influences of ENSO on the East Asian-western Pacific winter climate tied to different ENSO properties in CMIP5 models. *J. Clim.* **28**, 2187–2202 (2015).
16. Xie, S.-P. et al. Indo-western Pacific ocean capacitor and coherent climate anomalies in post-ENSO summer: a review. *Adv. Atmos. Sci.* **33**, 411–432 (2016).
17. Wang, B., Li, J. & He, Q. Variable and robust East Asian monsoon rainfall response to El Niño over the past 60 years (1957-2016). *Adv. Atmos. Sci.* **34**, 1235–1248 (2017).
18. Tao, W., Kong, X., Liu, Y., Wang, Y. & Dong, D. Diversity of Northwest Pacific atmospheric circulation anomalies during post-ENSO summer. *Front. Environ. Sci.* **10**, 1068155 (2022).
19. Wang, Y. et al. Correcting climate model sea surface temperature simulations with generative adversarial networks: Climatology, interannual variability, and extremes. *Adv. Atmos. Sci.* **41**, 1299–1312 (2024).
20. Gill, A. E. Some simple solutions for heat-induced tropical circulation. *Q. J. R. Meteorol. Soc.* **106**, 447–462 (1980).
21. Wu, B., Zhou, T. & Li, T. Atmospheric dynamic and thermodynamic processes driving the western North Pacific anomalous anticyclone during El Niño. Part I: maintenance mechanisms. *J. Clim.* **30**, 9621–9635 (2017).
22. Lau, N.-C. & Nath, M. J. Atmosphere-ocean variations in the Indo-Pacific sector during ENSO episodes. *J. Clim.* **16**, 3–20 (2003).
23. Gong, H. et al. The climatology and interannual variability of the East Asian winter monsoon in CMIP5 models. *J. Clim.* **27**, 1659–1678 (2014).
24. Jiang, W. et al. Biases and improvements of the ENSO-East Asian winter monsoon teleconnection in CMIP5 and CMIP6 models. *Clim. Dyn.* **59**, 2467–2480 (2022).
25. Lau, N.-C. & Nath, M. J. Impact of ENSO on the variability of the Asian-Australian monsoons as simulated in GCM experiments. *J. Clim.* **13**, 4287–4309 (2000).
26. Ham, Y., Kug, J. & Kang, I. Role of moist energy advection in formulating anomalous Walker circulation associated with El Niño. *J. Geophys. Res.* **112**, D24105 (2007).
27. Vecchi, G. A. & Soden, B. J. Global warming and the weakening of the tropical circulation. *J. Clim.* **20**, 4316–4340 (2007).
28. Yu, B., Zwiers, F. W., Boer, G. J. & Ting, M. F. Structure and variances of equatorial zonal circulation in a multimodel ensemble. *Clim. Dyn.* **39**, 2403–2419 (2012).
29. Bayr, T., Dommenget, D., Martin, T. & Power, S. B. The eastward shift of the Walker circulation in response to global warming and its relationship to ENSO variability. *Clim. Dyn.* **43**, 2747–2763 (2014).
30. Cai, W. et al. Increasing frequency of extreme El Niño events due to greenhouse warming. *Nat. Clim. Chang.* **4**, 111–116 (2014).
31. Huang, P. & Xie, S.-P. Mechanisms of change in ENSO-induced tropical Pacific rainfall variability in a warming climate. *Nat. Geosci.* **8**, 922–926 (2015).
32. Wang, Y., He, C. & Li, T. Response of the anomalous western North Pacific anticyclone during El Niño mature winter to global warming. *Clim. Dyn.* **54**, 727–740 (2020).
33. Barnett, T. P., Adam, J. C. & Lettenmaier, D. P. Potential impacts of a warming climate on water availability in snow-dominated regions. *Nature* **438**, 303–309 (2005).
34. Toggweiler, J. R. & Russell, J. Ocean circulation in a warming climate. *Nature* **451**, 286–288 (2008).
35. Rahmstorf, S. & Coumou, D. Increase of extreme events in a warming world. *Proc. Natl Acad. Sci. USA* **108**, 17905–17909 (2011).
36. Ma, J., Xie, S.-P. & Kosaka, Y. Mechanisms for tropical tropospheric circulation change in response to global warming. *J. Clim.* **25**, 2979–2994 (2012).
37. Wang, X., Jiang, D. & Lang, X. Future extreme climate changes linked to global warming intensity. *Sci. Bull.* **62**, 1673–1680 (2017).
38. Johnson, N. C., Xie, S.-P., Kosaka, Y. & Li, X. Increasing occurrence of cold and warm extremes during the recent global warming slowdown. *Nat. Commun.* **9**, 1724 (2018).
39. Studholme, J., Fedorov, A. V., Gulev, S. K., Emanuel, K. & Hodges, K. Poleward expansion of tropical cyclone latitudes in warming climates. *Nat. Geosci.* **15**, 14–28 (2022).
40. Kotz, M., Lange, S., Wenz, L. & Levermann, A. Constraining the pattern and magnitude of projected extreme precipitation change in a multi-model ensemble. *J. Clim.* **37**, 97–111 (2023).
41. Tang, H. et al. Human contribution to the risk of 2021 Northwestern Pacific concurrent marine and terrestrial summer heat. *Bull. Am. Meteorol. Soc.* **104**, E673–E679 (2023).
42. Peters, G. P. et al. The challenge to keep global warming below 2. *Nat. Clim. Chang.* **3**, 4–6 (2013).
43. Sanderson, B. M., O'Neill, B. C. & Tebaldi, C. What would it take to achieve the Paris temperature targets? *Geophys. Res. Lett.* **43**, 7133–7142 (2016).
44. Field, C. B. & Mach, K. J. Rightsizing carbon dioxide removal. *Science* **356**, 706–707 (2017).

45. Keller, D. P. et al. The carbon dioxide removal model intercomparison project (CDRMIP): rationale and experimental protocol for CMIP6. *Geosci. Model Dev.* **11**, 1133–1160 (2018).
46. Luderer, G. et al. Residual fossil CO_2 emissions in 1.5-2 °C pathways. *Nat. Clim. Chang.* **8**, 626–633 (2018).
47. Rogelj, J., Popp, A. & Calvin, K. V. Scenarios towards limiting global mean temperature increase below 1.5 °C. *Nat. Clim. Chang.* **8**, 325–332 (2018).
48. Realmonte, G. et al. An inter-model assessment of the role of direct air capture in deep mitigation pathways. *Nat. Commun.* **10**, 3277 (2019).
49. Held, I. M. et al. Probing the fast and slow components of global warming by returning abruptly to preindustrial forcing. *J. Clim.* **23**, 2418–2427 (2010).
50. Long, S.-M., Xie, S.-P., Zheng, X.-T. & Liu, Q. Fast and slow responses to global warming: sea surface temperature and precipitation patterns. *J. Clim.* **27**, 285–299 (2014).
51. Long, S.-M. et al. Effects of ocean slow response under low warming targets. *J. Clim.* **33**, 477–496 (2020).
52. Wu, P., Wood, R., Ridley, J. & Lowe, J. Temporary acceleration of the hydrological cycle in response to a CO_2 rampdown. *Geophys. Res. Lett.* **37**, L12705 (2010).
53. Cao, L., Bala, G. & Caldeira, K. Why is there a short-term increase in global precipitation in response to diminished CO_2 forcing? *Geophys. Res. Lett.* **38**, L06703 (2011).
54. Chadwick, R., Wu, P., Good, P. & Andrews, T. Asymmetries in tropical rainfall and circulation patterns in idealised CO_2 removal experiments. *Clim. Dyn.* **40**, 295–316 (2013).
55. Wu, P., Ridley, J., Pardaens, A., Levine, R. & Lowe, J. The reversibility of CO_2 induced climate change. *Clim. Dyn.* **45**, 745–754 (2015).
56. Kim, S.-K. et al. Widespread irreversible changes in surface temperature and precipitation in response to CO_2 forcing. *Nat. Clim. Chang.* **12**, 834–840 (2022).
57. Song, S.-Y. et al. Climate sensitivity controls global precipitation hysteresis in a changing CO_2 pathway. *npj Clim. Atmos. Sci.* **6**, 1–10 (2023).
58. Zhou, S., Huang, P., Xie, S.-P., Huang, G. & Wang, L. Varying contributions of fast and slow responses cause asymmetric tropical rainfall change between CO_2 ramp-up and ramp-down. *Sci. Bull.* **67**, 1702–1711 (2022).
59. Song, S.-Y. et al. Asymmetrical response of summer rainfall in East Asia to CO_2 forcing. *Sci. Bull.* **67**, 213–222 (2022).
60. Zhang, S., Qu, X., Huang, G. & Hu, P. Asymmetric response of South Asian summer monsoon rainfall in a carbon dioxide removal scenario. *npj Clim. Atmos. Sci.* **6**, 10 (2023).
61. Liu, C. et al. Hysteresis of the El Niño-Southern Oscillation to CO_2 forcing. *Sci. Adv.* **9**, eadh8442 (2023).
62. Yeh, S.-W. & Kirtman, B. P. ENSO amplitude changes due to climate change projections in different coupled models. *J. Clim.* **20**, 203–217 (2007).
63. Collins, M. et al. The impact of global warming on the tropical Pacific Ocean and El Niño. *Nat. Geosci.* **3**, 391–397 (2010).
64. Liu, Z. et al. Evolution and forcing mechanisms of El Niño over the past 21,000 years. *Nature* **515**, 550–553 (2014).
65. Cai, W. et al. ENSO and greenhouse warming. *Nat. Clim. Change* **5**, 849–859 (2015).
66. Maher, N., Matei, D., Milinski, S. & Marotzke, J. ENSO change in climate projections: forced response or internal variability? *Geophys. Res. Lett.* **45**, 11,390–11,398 (2018).
67. Zheng, X.-T., Hui, C. & Yeh, S.-W. Response of ENSO amplitude to global warming in CESM large ensemble: uncertainty due to internal variability. *Clim. Dyn.* **50**, 4019–4035 (2018).
68. Power, S., Delage, F., Chung, C., Kociuba, G. & Keay, K. Robust twenty-first-century projections of El Niño and related precipitation variability. *Nature* **502**, 541–545 (2013).
69. Chung, C. T. Y., Power, S. B., Arblaster, J. M., Rashid, H. A. & Roff, G. L. Nonlinear precipitation response to El Niño and global warming in the Indo-Pacific. *Clim. Dyn.* **42**, 1837–1856 (2014).
70. Power, S. B., Delage, F. P. D., Chung, C. T. Y., Ye, H. & Murphy, B. F. Humans have already increased the risk of major disruptions to Pacific rainfall. *Nat. Commun.* **8**, 14368 (2017).
71. Yan, Z. et al. Eastward shift and extension of ENSO-induced tropical precipitation anomalies under global warming. *Sci. Adv.* **6**, eaax4177 (2020).
72. Xie, X., Zhou, S., Zhang, J. & Huang, P. The role of background SST changes in the ENSO-driven rainfall variability revealed from the atmospheric model experiments in CMIP5/6. *Atmo. Res.* **261**, 105732 (2021).
73. Huang, P., Chen, D. & Ying, J. Weakening of the tropical atmospheric circulation response to local sea surface temperature anomalies under global warming. *J. Clim.* **30**, 8149–8158 (2017).
74. Yang, K. et al. Increased variability of the western Pacific subtropical high under greenhouse warming. *Proc. Natl Acad. Sci. USA* **119**, e2120335119 (2022).
75. Kug, J.-S. et al. Hysteresis of the intertropical convergence zone to CO_2 forcing. *Nat. Clim. Change* **12**, 47–53 (2022).
76. Grabowski, W. W. & Moncrieff, M. W. Moisture-convection feedback in the tropics. *Q. J. R. Meteorol. Soc.* **130**, 3081–3104 (2004).
77. Bony, S. & Emanuel, K. A. On the role of moist processes in tropical intraseasonal variability: cloud-radiation and moisture-convection feedbacks. *J. Atmos. Sci.* **62**, 2770–2789 (2005).
78. Bretherton, C. S. & Sobel, A. H. A simple model of a convectively coupled Walker circulation using the weak temperature gradient approximation. *J. Clim.* **15**, 2907–2920 (2002).
79. Su, H. & Neelin, J. D. Teleconnection mechanisms for tropical Pacific descent anomalies during El Niño. *J. Atmos. Sci.* **59**, 2694–2712 (2002).
80. Neelin, J. D. & Su, H. Moist teleconnection mechanisms for the tropical South American and Atlantic sector. *J. Clim.* **18**, 3928–3950 (2005).
81. Lau, W. K. M. & Tao, W. Precipitation-radiation-circulation feedback processes associated with structural changes of the ITCZ in a warming climate during 1980-2014: an observational portrayal. *J. Clim.* **33**, 8737–8749 (2020).
82. Hu, K. et al. Interdecadal variations in ENSO influences on northwest Pacific-East Asian early summertime climate simulated in CMIP5 models. *J. Clim.* **27**, 5982–5998 (2014).
83. Tao, W. et al. Interdecadal modulation of ENSO teleconnections to the Indian Ocean Basin Mode and their relationship under global warming in CMIP5 models. *Int. J. Climatol.* **35**, 391–407 (2015).
84. Sun, N. et al. Amplified tropical Pacific rainfall variability related to background SST warming. *Clim. Dyn.* **54**, 2387–2402 (2020).
85. Tokinaga, H., Xie, S.-P., Deser, C., Kosaka, Y. & Okumura, Y. M. Slowdown of the Walker circulation driven by tropical Indo-Pacific warming. *Nature* **491**, 439–443 (2012).
86. Power, S. B., Delage, F., Colman, R. & Moise, A. Consensus on twenty-first-century rainfall projections in climate models more widespread than previously thought. *J. Clim.* **25**, 3792–3809 (2012).
87. Bretherton, C. S., Widmann, M., Dymnikov, V. P., Wallace, J. M. & Bladé, I. The effective number of spatial degrees of freedom of a time-varying field. *J. Clim.* **12**, 1990–2009 (1999).
88. Neelin, J. D. & Held, I. M. Modeling tropical convergence based on the moist static energy budget. *Mon. Weather Rev.* **115**, 3–12 (1987).

Acknowledgements

We acknowledge the World Climate Research Program for its coordination and promotion of CMIP6, facilitated by the Working Group on Coupled Modelling. This work is supported by the National Natural Science Foundation of China (Grant Nos. 42141019, 42261144687, 42475048, 42175049, 42405041 and 42105032).

Author contributions

W.Z. designed the study, executed the data analyses, and authored the initial manuscript draft. W.T. contributed to the research design and revised the initial draft. W.T., G.H., K.H., X.Q., H.G., K.Y., and Y.W. participated in critical discussions and contributed to the finalization of the manuscript.

Competing interests

The authors declare no competing interests.

Additional information

Supplementary information The online version contains supplementary material available at https://doi.org/10.1038/s41612-024-00854-4.

Correspondence and requests for materials should be addressed to Weichen Tao or Gang Huang.